Bioactive Materials 25 (2023) 189–200

Contents lists available at ScienceDirect

Bioactive Materials

journal homepage: www.keaipublishing.com/en/journals/bioactive-materials

H_2O_2-responsive polymer prodrug nanoparticles with glutathione scavenger for enhanced chemo-photodynamic synergistic cancer therapy

Guanchun Wang [a], Yue Su [a], Xinliang Chen [b], Yongfeng Zhou [a], Ping Huang [a,**], Wei Huang [a,*], Deyue Yan [a]

[a] School of Chemistry and Chemical Engineering, Shanghai Jiao Tong University, Shanghai, 200240, China
[b] The International Peace Maternity and Child Health Hospital, School of Medicine, Shanghai Jiao Tong University, Shanghai, China

ARTICLE INFO

Keywords:
H_2O_2-responsiveness
Alternating copolymer prodrug
GSH-scavenger
Photosensitizer
Chemo-photodynamic synergistic cancer therapy

ABSTRACT

The combination of chemotherapy and photodynamic therapy (PDT) based on nanoparticles (NPs) has been extensively developed to improve the therapeutic effect and decrease the systemic toxicity of current treatments. However, overexpressed glutathione (GSH) in tumor cells efficiently scavenges singlet oxygens ($^1O_2$) generated from photosensitizers and results in the unsatisfactory efficacy of PDT. To address this obstacle, here we design H_2O_2-responsive polymer prodrug NPs with GSH-scavenger (Ce6@P(EG-*a*-CPBE) NPs) for chemo-photodynamic synergistic cancer therapy. They are constructed by the co-self-assembly of photosensitizer chlorin e6 (Ce6) and amphiphilic polymer prodrug P(EG-*a*-CPBE), which is synthesized from a hydrophilic alternating copolymer P(EG-*a*-PD) by conjugating hydrophobic anticancer drug chlorambucil (CB) via an H_2O_2-cleavable linker 4-(hydroxymethyl)phenylboronic acid (PBA). Ce6@P(EG-*a*-CPBE) NPs can efficiently prevent premature drug leakage in blood circulation because of the high stability of the PBA linker under the physiological environment and facilitate the delivery of Ce6 and CB to the tumor site after intravenous injection. Upon internalization of Ce6@P(EG-*a*-CPBE) NPs by tumor cells, PBA is cleaved rapidly triggered by endogenous H_2O_2 to release CB and Ce6. Ce6 can effectively generate abundant $^1O_2$ under 660 nm light irradiation to synergistically kill cancer cells with CB. Concurrently, PBA can be transformed into a GSH-scavenger (quinine methide, QM) under intracellular H_2O_2 and prevent the depletion of $^1O_2$, which induces the cooperatively strong oxidative stress and enhanced cancer cell apoptosis. Collectively, such H_2O_2-responsive polymer prodrug NPs loaded with photosensitizer provide a feasible approach to enhance chemo-photodynamic synergistic cancer treatment.

1. Introduction

Over the past few decades, polymeric nanoparticles as promising potential drug delivery vehicles have been widely developed for cancer chemotherapy since they can overcome several biological barriers during cargo delivery, such as poor water solubility, rapid blood clearance, severe side effects, low tumor tissue accumulation, and so on [1–3]. Although great progress has been achieved, these drug delivery systems relied on the physical encapsulation of drugs in polymeric nanoparticles during the self-assembly process still face two major drawbacks that limit their better therapeutic effect [4]. On the one hand, polymeric nanoparticles have very low drug loading capacity, usually less than 5% [5,6]. On the other hand, drug-loaded formulation usually encounters inevitable drug leakage during blood circulation causing unpredictable systemic cytotoxicity [7,8]. To address these problems, an attractive strategy is to directly covalent conjugation of a hydrophobic drug to the hydrophilic polymer via a tumor microenvironment responsive linkage that is stable in the blood to form polymer-drug conjugate, also called polymeric prodrug, which was first reported by the seminal work of Ringsdorf in 1975 [9]. After that, some different polymer-drug conjugates have been developed and later tested in clinical trials [10–12]. Since these pioneering efforts, the field of polymer-drug conjugates has acquired tremendous development.

As an ideal polymer-drug conjugate for cancer chemotherapy, it should be stable in blood circulation to avoid drug leakage and reduce side-effect to normal tissues. Once it is internalized by cancer cells, the

Peer review under responsibility of KeAi Communications Co., Ltd.
* Corresponding author.
** Corresponding author.
E-mail addresses: hp158@sjtu.edu.cn (P. Huang), hw66@sjtu.edu.cn (W. Huang).

https://doi.org/10.1016/j.bioactmat.2023.01.026
Received 23 November 2022; Received in revised form 27 January 2023; Accepted 31 January 2023

polymeric prodrug should be quickly degraded triggered by the intracellular microenvironment to release enough drugs in cancer cells to effectively kill the cells. Therefore, to realize the mentioned above, various stimuli-sensitive linkers that can be specifically cleaved under triggering by internal stimuli (e.g., pH [13,14], enzyme [15–17], redox [18–22], etc.) have been intensively explored to conjugate polymer with the drug to obtain smart polymeric prodrug. Among these stimuli, ROS-responsiveness has attracted much attention in the construction of polymeric prodrugs for cancer chemotherapy due to overproducing ROS around mitochondria in cancer cells. Recently, various ROS-induced cleavable chemical bonds, including phenylboronic esters/acids [23–25], thioketals [26–28], diselenium [29–31], and aryl oxalate ester [32–34] have been exploited and widely used to construct ROS-triggered polymeric prodrug for controlled intracellular drug release and selective cancer chemotherapy.

Moreover, to achieve a better therapeutic effect, one opinion is to combine chemotherapy and PDT (an advanced noninvasive therapeutic method that has been widely used to treat various cancers in the clinic). The primary principle of PDT is to generate large amounts of cytotoxic ROS, such as singlet oxygen ($^1O_2$), by using photosensitizers under light irradiation to kill cancer cells [35–38]. Utilizing this property, researchers have developed various ROS-responsive polymeric prodrugs to deliver photosensitizer to tumor sites for combined chemotherapy and photodynamic therapy of cancer under light irradiation, in which the $^1O_2$ generated from photosensitizer could not only cleave the ROS-sensitive linker to release the anticancer drug but also directly kill the cancer cells [39]. For example, Pei and co-workers developed polyphosphoester-doxorubicin polymeric prodrug through ROS-cleavable thioketal (TK) linkage for the combination of chemo-photodynamic therapy [40]. Chu and co-workers reported a ROS-responsive MPEG-(TK-CPT)-PPa prodrug delivery system for combined chemotherapy and photodynamic therapy [41]. However, in these reported systems, the $^1O_2$ produced from photosensitizer could be consumed by a high concentration of GSH in cancer cells, which greatly reduces the effect of PDT and limits its applications in the clinic [42]. To overcome the obstacle, it is highly expected that the development of multifunctional polymeric nano-prodrug systems could effectively achieve controllable intracellular drug release and simultaneously rapidly decrease the level of GSH in cancer cells to avoid the depletion of $^1O_2$. As reported, phenylboronic acid/ester moieties-containing materials could be converted into toxic quinone methide (QM) triggered by H_2O_2 in cancer cells. QM is capable of rapidly alkylating GSH, causing GSH depletion and inhibiting the antioxidative capability of cancer cells [43–46]. Therefore, using phenylboronic acid as a linker to fabricate ROS-sensitive polymeric prodrug to load and deliver photosensitizer for chemo-photodynamic therapy would be of significant interest.

Aiming at this goal, we designed and constructed some H_2O_2-responsive polymer prodrug NPs loaded with Ce6 for enhanced chemo-photodynamic synergistic cancer therapy (Scheme 1). The hydrophobic anticancer drug CB was conjugated to the hydrophilic alternating copolymer P(EG-*a*-PD) via an H_2O_2-cleavable linker PBA to form an amphiphilic alternating copolymer prodrug P(EG-*a*-CPBE), which could co-self-assemble into NPs with the photosensitizer Ce6 in water. The obtained Ce6@P(EG-*a*-CPBE) NPs could efficiently avoid premature drug leakage in the blood circulation due to the high stability of the PBA linker under the physiological environment and accumulate at the tumor site via the enhanced permeability and retention (EPR) effect. Once the internalization of NPs by tumor cells, the linker PBA could be rapidly cleaved triggered by endogenous H_2O_2 to release CB and Ce6 and simultaneously converted into QM, which could quickly scavenge intracellular GSH and prevent the depletion of $^1O_2$ generated from Ce6 under 660 nm light irradiation. Finally, H_2O_2-responsive Ce6@P(EG-*a*-CPBE) NPs with GSH-scavenger under light irradiation can effectively enhance chemo-photodynamic synergistic cancer treatment.

2. Materials and methods

2.1. Materials

N,*N*′-dicyclohexylcarbodiimide (DCC, 99%, Adamas), Poly(ethylene glycol) diglycidyl ether (M_n = 500, PEGDGE-9, Sigma-Aldrich), 3-amino-1,2-propanediol (APD, 98%, Adamas), Nile red (NR, 99%, Acros), 4-(dimethylamino)pyridine (DMAP, 99%, Adamas), 4-(hydroxymethyl)phenylboronic acid pinacol ester (PBAPE, 98%, Adamas),

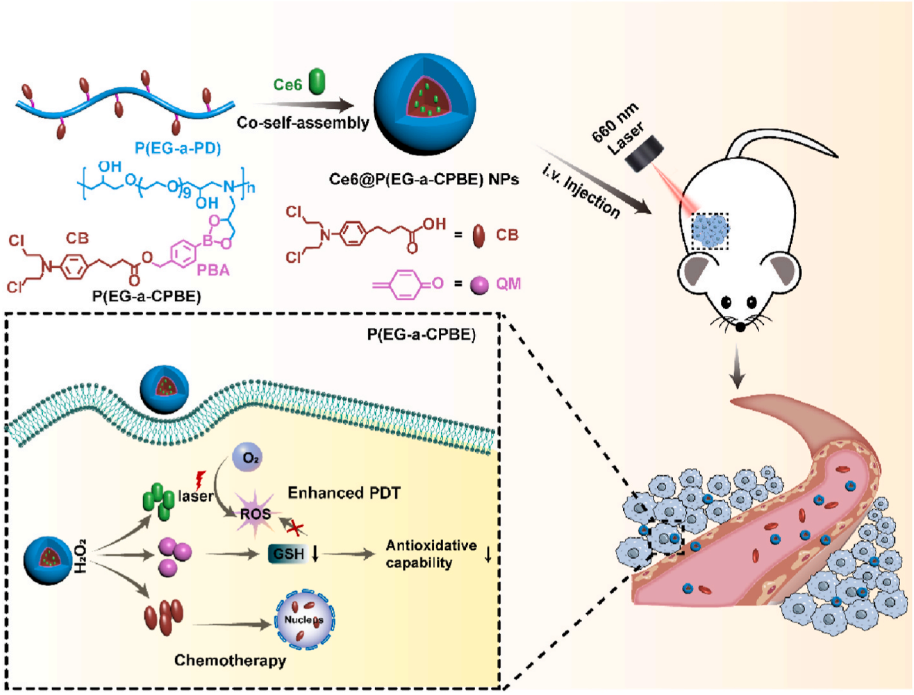

Scheme 1. Schematic illustration of the construction of H_2O_2-responsive Ce6@P(EG-*a*-CPBE) NPs with GSH-scavenger, drug delivery, and the intracellular release of CB and Ce6 for enhanced chemo-photodynamic synergistic cancer therapy.

chlorambucil (CB, 98%, Yuanye Bio-Technology), sodium periodate ($NaIO_4$, 99%, Adamas), molecular sieves (Adamas), chlorin e6 (Ce6, 97%, Alfa), methylthiazolyldiphenyl-tetrazolium bromide (MTT, Beyotime), acetone (99.9%, Greagent), ethanol (95%, Greagent) and dimethyl sulfoxide (DMSO, 99.9%, Greagent) were directly used without further purification.

2.2. Synthesis of alternating copolymer prodrug P(EG-*a*-CPBE)

4-(hydroxymethyl) phenylboronic acid-modified chlorambucil (CPBA) (1.50 g, 3.42 mmol), P(EG-*a*-PD) (1.99 g, 0.166 mmol) and ultradry DMSO (30 mL) were added in a three-neck round bottom flask with a small amount of molecular sieve. Then the solution was stirred at 60 °C for 30 h under N_2. The mixture solution was centrifuged at 10,000 rpm for 10 min and then dialyzed with DMSO for one day and deionized water for 1 day (MWCO = 7000 g mol^{-1}). The resultant product was lyophilized to give a light brown solid. The drug content of P(EG-*a*-CPBE) was determined by HPLC analysis according to the standard curve of CB in ethanol tested via the HPLC spectrum. And the CB content was calculated as follows:

$$CB\ content\ (wt\%) = \frac{weight\ of\ Cb\ in\ polymeric\ prodrug}{weigh\ of\ polymeric\ prodrug} \times 100\%$$

2.3. Preparation of P(EG-*a*-CPBE) NPs

Briefly, P(EG-*a*-CPBE) prodrug (20.0 mg) and DMSO (0.5 mL) were added into 1 mL centrifuge tube. After complete dissolution, the solution was added dropwise into 5 mL of deionized water. After stirring for 3 min, the mixture was transferred into the dialysis bag and dialyzed with deionized water for 16 h (MWCO = 1000 g mol^{-1}) and the P(EG-*a*-CPBE) NPs solution was obtained.

2.4. Preparation of Ce6-loaded P(EG-*a*-CPBE) NPs

Typically, Ce6 (2 mg), P(EG-*a*-CPBE) (20 mg), and DMSO (0.5 mL) were added into 1 mL centrifuge tube and shocked at r.t. for 5 min to allow complete dissolution. Then the mixture was added dropwise into 5 mL of deionized water. After slightly stirring for 2 min, the solution was dialyzed by use of deionized water for 16 h (MWCO = 1000 g mol^{-1}). To determine the amount of Ce6, the Ce6@P(EG-*a*-CPBE) NPs solution was frozen and dried under vacuum and then re-dissolved with DMSO. The Ce6 content was determined by the use of UV–vis spectrophotometer at 406 nm absorbance.

2.5. Prodrug NPs stability

P(EG-*a*-CPBE) NPs and Ce6@ P(EG-*a*-CPBE) NPs were added in PBS with 10% FBS or PBS placed at 4 °C in a refrigerator for 5 days. At the predetermined time (0, 1, 2, 3, 4, and 5 d), the average diameters were measured by DLS.

2.6. In vitro cellular uptake of Ce6@P(EG-*a*-CPBE) NPs

The cellular uptake behaviors of Ce6@P(EG-*a*-CPBE) NPs were evaluated against MCF-7 cells. For flow cytometry, the 6-well plate was seeded with 5.0×10^5 MCF-7 cells per well and cultured overnight. Then the fresh DMEM was used to dilute the solution of Ce6@P(EG-*a*-CPBE) NPs to a final concentration of Ce6 (1 μg mL^{-1}), which was added to different wells. After incubating at 37 °C for 1, 2, and 4 h, the DMEM culture was removed and cold PBS was used to wash the cells three times. After treatment with trypsin, the fluorescence of Ce6 in cells was analyzed by using BD LSRFortessa flow cytometer. For the confocal laser scanning microscopy (CLSM) study, 1.2×10^6 MCF-7 cells were equally seeded in a 6-well plate and incubated for 24 h, followed by removing the mixture and adding Ce6@P(EG-*a*-CPBE) NPs solutions at the concentration of Ce6 (1 μg mL^{-1}). After incubation for 4 h, the DMEM was removed and PBS was used to wash the cells two times. Subsequently, the cells were treated with 1 mL formaldehyde (4%) for 20 min in dark and rinsed with PBS three times. Finally, 5 μg mL^{-1} Hoechst 33,342 (0.5 mL) was used to stain the cell nuclear for 5 min. The fluorescence images of cells were taken by LEICA TCS SP8 fluorescence microscopy.

2.7. In vitro ROS production and GSH content

ROS assay kit was utilized to determine the ROS generation ability of Ce6@P(EG-*a*-CPBE) inside cells. Briefly, MCF-7 cells were seeded in a cover glassed bottom dish with 2×10^4 cells per well. After growth for 12 h, the cells were treated with Ce6@P(EG-*a*-CPBE) for 4 h. The mixture solution was removed and PBS was used to rinse the cells three times. Then 2 mL of fresh DMEM containing DCFH-DA (dichlorofluorescein-diacetate) (10 μM) was added, and the cells were cultured for 20 min. After that, the medium was removed and the cells were rinsed by use of serum-free DMEM three times and irradiated by a 660 nm laser for 10 min and further cultured with complete DMEM for 4 h. Subsequently, the cells were treated according to the method as described in the **2.6**. The untreated and unirradiated cells were used as control.

GSH assay kit was used to measure the relative GSH concentration in MCF-7 cells. Briefly, a density of 3.0×10^5 MCF-7 cells per well was seeded in 6-well plant. After 12 h growth, the cells were added with PBS, CB, Ce6@P(EG-*a*-CPBE) NPs and further cultured for 24 h. After that, the cells were irradiated by a 660 nm laser for 10 min. Subsequently, the mixture solution was removed carefully and the cells were rinsed by using PBS twice. The cells unirradiated cells were used as control. Finally, these samples were treated following the protocol, and the absorbance at 420 nm was detected by Bio-Tek Synergy H4.

2.8. In vitro cell cytotoxicity

The cell cytotoxicity of Ce6@P(EG-*a*-CPBE) was evaluated against MCF-7 cells by MTT assay. Briefly, 200 μL of complete DMEM containing 8×10^3 MCF-7 cells were seeded in 96-well plate. After growth for 12 h, the medium was replaced with 200 μL of DMEM containing different concentrations of CB or Ce6. For the laser irradiation group, after treatment for 12 h, the DMEM was removed and the cells were washed with PBS two times. After adding the fresh DMEM, the cells were irradiated by a 660 nm laser for 10 min. After that, the cells were further grown for 72 h at 37 °C. The cells treated with Vitamin C (V_C) were used as a control. For the groups without laser, the cells were directly incubated for 72 h at 37 °C. Finally, the 96-well plate was added to the MTT solution (20 μL) and incubated for another 4 h. After removing the mixture solution, 200 μL DMSO was added to each well to dissolve the formazan crystals. Then the absorbance at 490 nm was recorded by the use of a microplate reader.

2.9. Cell apoptosis assay

2 mL DMEM per well containing 5.0×10^5 MCF-7 cells was added into 6-well plate and cultured overnight. Then the cells were incubated with PBS, free CB, or Ce6@P(EG-*a*-CPBE). For the laser irradiation group, after treatment for 12 h, the DMEM was removed and the cells were washed by using cold PBS two times. After adding the fresh DMEM, the cells were irradiated by a 660 nm laser for 10 min. After that, the cells were further cultivated for another 12 h at 37 °C. For the groups without laser irradiation, the cells were directly treated for 24 h at 37 °C. Then the cells were collected and centrifuged at 1000 rpm for 3 min. The cold PBS was used to wash the cells and stained them with FITC-Annexin V and PI for 15 min. Finally, these samples were detected by flow cytometry, and 1×10^4 events per sample were collected.

2.10. Pharmacokinetics and biodistribution

The mice with MCF-7 tumor-bearing were injected with free CB or Ce6@P(EG-*a*-CPBE) NPs at a CB dose of 10 mg kg^{-1} (n = 3 per group) via the tail vein. At predetermined time points, the blood was taken from the eye socket after injection. The plasma was obtained by centrifugation of the blood for 10 min and extracted with 200 μL CH_2Cl_2 two times. The amounts of CB in the plasma were measured according to our previously reported method. To assess the tissue distribution, the samples as the same above were injected into the MCF-7 tumor-bearing mice via tail vein, respectively. The mice were sacrificed at 2 h, and 8 h after drug injection, and the tumor and main organs were taken out. The concentration of CB in the tumor and main organs were analyzed according to our previous work.

2.11. In vivo optical imaging

The MCF-7 tumor-bearing mice were intravenously injected with 200 μL of Ce6@P(EG-*a*-CPBE) NPs or free Ce6, respectively. The fluorescence distribution in MCF-7 tumor-bearing mice was detected at 1, 2, 4, 8, and 24 h using a Kodak multimode imaging system with the wavelength (λex = 635 nm, λem = 660 nm). At the end of the test, the mice were sacrificed, and the tumor tissues and main organs were stripped to use for ex vivo imaging under a Kodak multimode imaging system.

2.12. In vivo anticancer activity

MCF-7 tumor-bearing mice (n = 5 per group) were intravenously injected with 200 μL of PBS, free CB, or Ce6@P(EG-*a*-CPBE) NPs at the dosage of CB (15 mg kg^{-1}) and Ce6 (1.36 mg kg^{-1}), respectively. These different formulations were injected into mice via the tail vein once every 3 days for 24 days. After every injection for 2 h, the tumor site of mice was irradiated by a 660 nm laser for 10 min, the group without irradiation was used as a control. The size of the tumor and the body weight of the mice were measured before every injection. The volume (V) of the tumor was calculated according to the formula: V (mm^3) = 1/2 × length (mm) × width $(mm)^2$. After 24 days of treatment, the mice were sacrificed and the tumors were stripped out, weighed, and photographed.

2.13. Statistical analysis

All acquired data were shown as mean ± SD. The statistical significance was analyzed using Student's t-test calculated by prism software; $^*P < 0.05$, $^{**}P < 0.01$, and $^{***}P < 0.001$ were deemed statistically significant in all analyses.

3. Results and discussion

3.1. Synthesis of P(EG-a-CPBE) prodrug

The amphiphilic alternating copolymer prodrug P(EG-*a*-CPBE) containing H_2O_2-responsive PBA linkage was synthesized according to the route in Scheme S1. The CB derivative (CPBA) was prepared from CB and 4-hydroxyphenyl boronic acid pinacol ester (PBAPE) by two-step reaction as shown in Scheme S1A. Firstly, PBAPE- modified CB (CPBAPE) was synthesized through esterification using DCC/DMAP. Secondly, the derivative CPBA was obtained through the deprotection of pinacol boronate esters in the presence of an acid catalyst. The ^{1}H NMR, LC-MS, and FTIR spectra of CPBA confirmed its chemical structure (Figs. S1 and S2). The P(EG-*a*-PD) was prepared according to our previous reports [47,48]. As shown in Scheme S1B, PEGDGE-9 and APD were selected as two monomers to polymerize at room temperature by the one-step amine-epoxy click reaction. The ^{1}H NMR, FTIR, GPC, and DCS techniques were used to confirm the chemical structure of P (EG-*a*-PD). As exhibited in Fig. S3, compared to the ^{1}H NMR spectrum of PEGDGE-9 in D_2O, the signal at 2.70 ppm (1), 2.88 ppm (1′), and 3.27 ppm (2) of the epoxy protons of PEGDGE-9 disappeared completely, while the two signals at 2.54 ppm (B) and 3.74 ppm (E) attributed to the methylene (-N-C**H**$_2$-CH(OH)–CH_2-) and the methine (-N–CH_2–C**H**(OH)–CH_2-) appeared in the ^{1}H NMR spectrum of P(EG-*a*-PD). In addition, the corresponding protons signals in the ^{1}H NMR spectrum of APD could be also observed in the ^{1}H NMR spectrum of P(EG-*a*-PD). The unimodal GPC trace of P(EG-*a*-PD) was displayed in Fig. 1A, suggesting the success of the amine-epoxy click polymerization. The DSC, FTIR spectrum, and TGA curves of P(EG-*a*-PD) were studied and shown in Fig. S4 and Figs. S5A and B. All these results demonstrated that the P(EG-*a*-PD) was synthesized successfully.

Phenylboronic acids are capable of binding diols to form phenylboronic esters that exhibit fast oxidation-responsive in the presence of H_2O_2 [49,50]. P(EG-*a*-CPBE) prodrug was obtained by a coupling reaction of the boronic acid group on CPBA and the diol on P(EG-*a*-PD) at 60 °C for 48 h with molecular sieves (Scheme S1C). As displayed in Fig. 1A, the GPC trace of P(EG-*a*-CPBE) prodrug significantly shifted to the high molecular weight side compared to that of P(EG-*a*-PD), suggesting CPBA was conjugated to P(EG-*a*-PD) successfully. Compared to the ^{1}H NMR spectrum of CPBA in Fig. 1B, the proton signals of CPBA at 8.25 (j), 7.51 (i), 7.10 (d), 6.68 (c), 5.23 (h), 2.60 (e), 2.44 (g), and 1.98 (f) ppm were changed to 7,61 (j'), 7.25 (i'), 7.05 (d'), 6.62 (c'), 5.10 (h'), 2.56 (e'), 2.37 (g'), and 1.94 (f') ppm, respectively, in the ^{1}H NMR spectrum of P(EG-*a*-CPBE). Meanwhile, the corresponding proton signals of P(EG-*a*-PD) also appeared in the ^{1}H NMR spectrum of P (EG-*a*-CPBE). The UV–vis absorption and FTIR spectra of P(EG-*a*-CPBE) were shown in Fig. 1C and Fig. S5, respectively. No obvious UV–vis absorption appeared in the absorption of P(EG-*a*-PD), while UV–vis absorption similar to the absorption of CB could be observed in the absorption of P(EG-*a*-CPBE). As shown in Fig. S5, a strong C═O stretching absorption band at 1730 cm^{-1} belonging to the ester of CPBA can be observed in the FTIR spectrum of P(EG-*a*-CPBE). Additionally, a strong -C-O-C- stretching absorption band at 1103 cm^{-1} belongs to P (EG-*a*-PD) and also appears in the FTIR spectrum of P(EG-*a*-CPBE). All these results demonstrated that CPBA was conjugated onto P(EG-*a*-PD) successfully. The CPBA content in the P(EG-*a*-CPBE) prodrug was 37.3% determined according to the standard curve of CPBA.

3.2. Preparation of the prodrug NPs

The hydrophobic CPBA was conjugated onto hydrophilic alternating copolymer P(EG-*a*-PD) to form amphiphilic P(EG-*a*-CPBE) prodrug that could self-assemble into NPs in water. The average size and morphology of the P(EG-*a*-CPBE) NPs were tested by DLS and TEM, respectively. As exhibited in Fig. 2A, the average diameter of P(EG-*a*-CPBE) NPs is 68.7 and the PDI (polydispersity index) is 0.209. The TEM photo of the NPs in Fig. 2B indicates that the P(EG-*a*-CPBE) prodrug can form spherical nanoparticles with an average size of approximate 61.2 nm, which is a little smaller than the DLS results. This can be ascribed to the shrinkage of NPs during the sample drying process. To further verify the self-assembly behavior of P(EG-*a*-CPBE) prodrug, the critical aggregation concentration (CAC) was determined by using Nile red. The relationship between the NR fluorescence intensity and the concentration of P(EG-*a*-CPBE) prodrug is displayed in Fig. 2C. The CAC of the P(EG-*a*-CPBE) prodrug is about 55.3 μg mL^{-1} from the inflection of the curve. DLS was used to monitor the stability of P(EG-*a*-CPBE) NPs in phosphate buffered saline (PBS) or PBS containing fetal bovine serum (FBS, 10%) for 5 days. As shown in Fig. 2D, the diameters of P(EG-*a*-CPBE) NPs increase a little after adding 10% FBS. No obvious change in size (Fig. 2D) and PDI (Fig. S7) is detected even after 5 days of storage, suggesting the good stability of P(EG-*a*-CPBE) NPs in the presence of serum.

The *in vitro* drug release properties of P(EG-*a*-CPBE) NPs were studied by dialysis in PBS (pH 7.4) containing (or not) 100 μM H_2O_2 at 37 °C. The cumulative release curves display that the concentration of

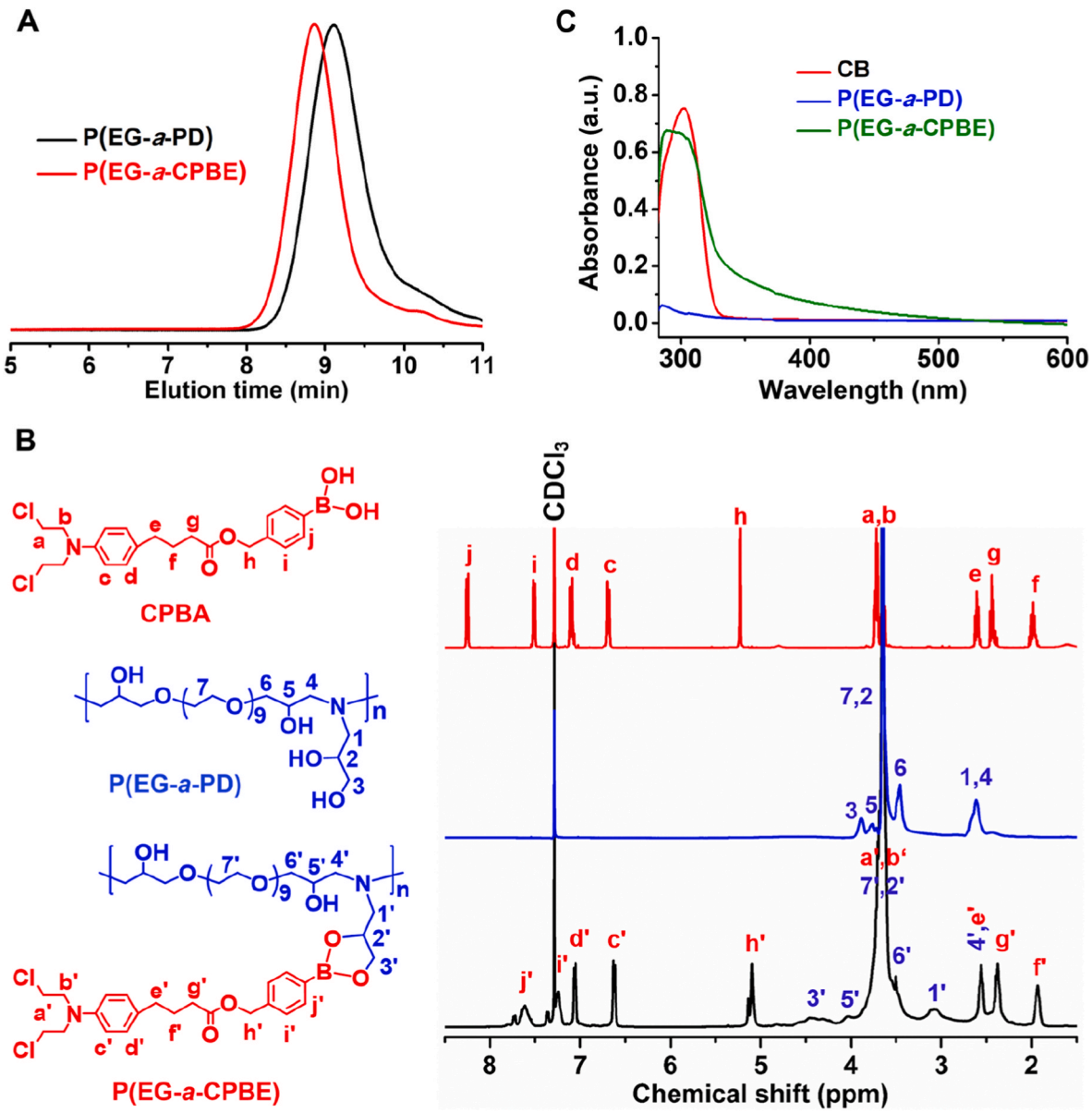

Fig. 1. The chemical characterization of P(EG-*a*-CPBE) prodrug. (**A**) GPC traces of P(EG-*a*-PD) and P(EG-*a*-CPBE) prodrug. (**B**) ^{1}H NMR spectra of CPBA, P(EG-*a*-PD) and P(EG-*a*-CPBE) prodrug in $CDCl_3$. (**C**) UV–vis spectra of CB, P(EG-*a*-PD), and P(EG-*a*-CPBE) prodrug in acetonitrile.

released CB is very low (about 9% at 48 h) in absence of H_2O_2 (Fig. 2E). However, incubation with 100 μM H_2O_2, the total release content of CB is accelerated significantly, and up to about 52% for 48 h. The result demonstrates that the linker PBA can be cleaved effectively triggered by H_2O_2. Moreover, after incubation with H_2O_2, the PBA linker can be changed into QM which has been confirmed to rapidly generate hydroxybenzyl alcohol (HA) with nucleophilic H_2O as shown in Fig. S8A [43,46]. The oxidation products of P(EG-*a*-CPBE) prodrug were confirmed by ^{1}H NMR spectrum as shown in Fig. S8B. The new peaks appear at 7.14 ppm (a), 6.72 ppm (b), and 4.32 ppm (c) belonging to the HA in the ^{1}H NMR spectrum of oxidation products as consistent with the previous reports [44,51,52], suggesting that H_2O_2-triggered QM release and the potential of P(EG-*a*-CPBE) NPs to rapidly alkylate GSH, causing apoptotic cell death. To further study the H_2O_2-triggered prodrug release, the changes of P(EG-*a*-CPBE) NPs in diameter and morphology after treatment with 100 μM H_2O_2 were investigated by use of DLS and TEM as displayed in Fig. 2F and Fig. S9. It can be seen that the average hydrodynamic diameter of P(EG-*a*-CPBE) NPs decreases significantly from 68.7 nm to 3.8 nm after incubation with H_2O_2 for 72 h. Meanwhile, only some small particles less than 10 nm can be observed in the TEM image (Fig. S9). These results indicate that the PBA linker cleavage is triggered by H_2O_2, which leads to the destruction of P(EG-*a*-CPBE) NPs.

The Ce6-loaded NPs (Ce6@P(EG-*a*-CPBE) NPs) were prepared by the co-self-assembly of Ce6 and P(EG-*a*-CPBE) prodrug in water. Compared with P(EG-*a*-CPBE) NPs, the average diameter of Ce6@P(EG-*a*-CPBE) NPs is slightly larger about 75.5 nm in an aqueous solution (Fig. 2A). The similar result can be observed from the TEM image of Ce6@P(EG-*a*-CPBE) NPs (Fig. 2G). Additionally, the Ce6@P(EG-*a*-CPBE) NPs have the same stability as P(EG-*a*-CPBE) NPs in PBS or PBS containing 10% FBS (Fig. 2D). Compared to the UV–vis absorption of free Ce6 (Fig. 2H), a slight redshift in the absorption of the Ce6@P(EG-*a*-CPBE) NPs is observed, which can be attributed to the result of intermolecular π–π stacking between CPBA and Ce6, further enhancing the stability of Ce6@P(EG-*a*-CPBE) NPs. Meanwhile, the loading content and efficiency of Ce6 in Ce6@P(EG-*a*-CPBE) NPs is 3.38% and 34.98% at the feed ratio of 10:1 (P(EG-*a*-CPBE)/Ce6, wt./wt.), respectively, which is calculated via the standard curve of Ce6 determined by use of UV–vis absorption. According to our design, the Ce6 in Ce6@P(EG-*a*-CPBE) NPs would be

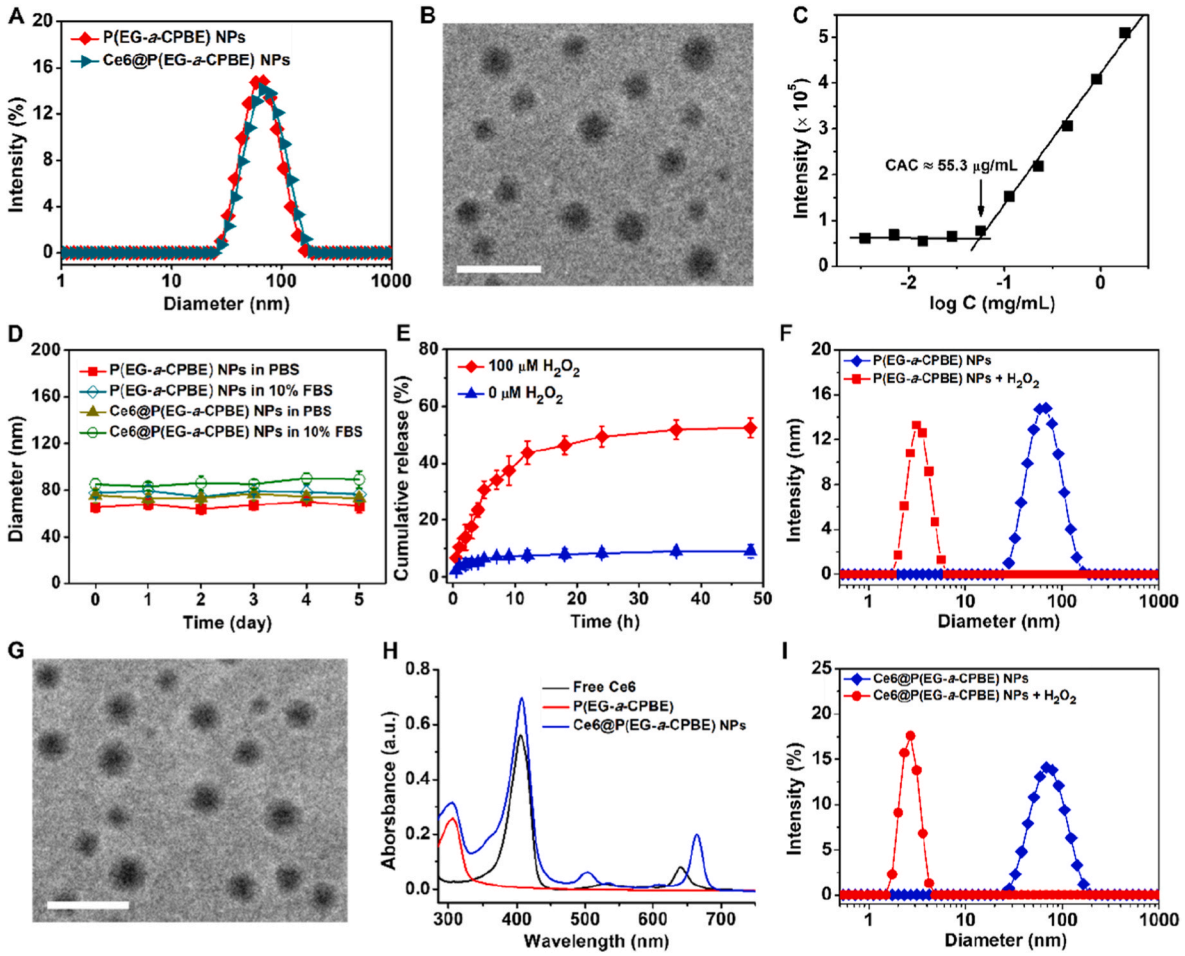

Fig. 2. Preparation and characterization of the Ce6@P(EG-*a*-CPBE) NPs. (**A**) DLS curve of P(EG-*a*-CPBE) NPs and Ce6@P(EG-*a*-CPBE) NPs. (**B, G**) TEM images of P(EG-*a*-CPBE) NPs (**B**) and Ce6@P(EG-*a*-CPBE) NPs (**G**). Scale bar: 200 nm. (**C**) The curve of NR fluorescent intensity vs P(EG-*a*-CPBE) prodrug concentration in water. The value of CAC is about 55.3 μg mL^{-1}. (**D**) The stability of P(EG-*a*-CPBE) NPs and Ce6@P(EG-*a*-CPBE) NPs in PBS or PBS containing 10% FBS. (**E**) CB release profiles from P(EG-*a*-CPBE) NPs with or without 100 μM H_2O_2 in PBS (pH 7.4). (**F, I**) DLS curves of P(EG-*a*-CPBE) NPs (**F**) and Ce6@P(EG-*a*-CPBE) NPs (**I**) before and after treatment with 100 μM H_2O_2. (**H**) UV–vis absorption spectra of Ce6@P(EG-*a*-CPBE) NPs and the control formulations.

released via the rapid cleavage of the PBA linker in the P(EG-*a*-CPBE) prodrug triggered by H_2O_2. The Ce6@P(EG-*a*-CPBE) NPs after treatment with 100 μM H_2O_2 were investigated by DLS and TEM. Similar results as that of P(EG-*a*-CPBE) NPs treated with H_2O_2 were obtained as shown in Fig. 2I and Fig. S9, suggesting that the nanostructure of Ce6@P(EG-*a*-CPBE) NPs is damaged, leading to the release of Ce6. To determine the ROS generation ability of Ce6@P(EG-*a*-CPBE) NPs under 660 nm laser irradiation, a ROS fluorescent quencher, 1,3-diphenylisobenzofuran (DPBF), was used to measure qualitatively based on the fluorescence intensity change of DPBF. As indicated in Fig. S10, the fluorescence intensity of DPBF solution containing Ce6@P(EG-*a*-CPBE) NPs decreases gradually with the laser irradiation time, which suggests Ce6@P(EG-*a*-CPBE) NPs can generate ROS effectively under the irradiation of 660 nm laser.

3.3. *In vitro* studies

To confirm Ce6@P(EG-*a*-CPBE) NPs can enter cells effectively, flow cytometry and CLSM were used to evaluate the cell internalization behavior. As seen in Fig. 3A, the fluorescence intensity of Ce6 in cells increases gradually with the incubation time. From the CLSM images (Fig. 3B), it can be shown that Ce6@P(EG-*a*-CPBE) NPs can be efficiently internalized into MCF-7 cells for 4 h-incubation. According to the merged image, the red fluorescence of Ce6 is mainly distributed in the cytoplasm. After the internalization of Ce6@P(EG-*a*-CPBE) NPs, the ROS generation capability in MCF-7 cells under 660 nm laser irradiation was evaluated by the use of DCFH-DA as a fluorescent probe [53]. The MCF-7 cells without treatment and irradiation were used as control. The nuclei were treated with Hoechst 33,342 for 5 min and then the cells were examined using a LEICA TCS SP8. As seen from CLSM images (Fig. 3C), the weak green fluorescence in cells can be observed after incubation by PBS, which may be ascribed to the intrinsic ROS in cells. While adding Ce6@P(EG-*a*-CPBE) NPs without 660 nm laser treatment, the intensity of green fluorescence in cells slightly increases, which should be attributed to the generated QM from P(EG-*a*-CPBE) prodrug depleting GSH to decrease the antioxidative ability, thus increasing the intracellular ROS concentration. Upon irradiation by 660 nm laser, the intensity of green fluorescence in cells can be observed significantly increase due to the $^1O_2$ generated from Ce6 under irradiation to improve the ROS concentration in cells. To study the GSH-scavenger capability of P(EG-*a*-CPBE) NPs, we investigated the effect of P(EG-*a*-CPBE) NPs on the level of GSH in MCF-7 cells. First, the cells were treated with various formulations, and then the level of GSH in MCF-7 cells was quantitatively measured by using the GSH/GSSG Assay Kit. As exhibited in Fig. 3D, the level of GSH both in MCF-7 cells treated with Ce6@P(EG-*a*-CPBE) NPs (L-) and Ce6@P(EG-*a*-CPBE) NPs (L+) reduces significantly, suggesting the QM released from the degradation of PBA linker in P(EG-*a*-CPBE) prodrug could effectively deplete the intracellular GSH. Meanwhile, the level of GSH in CB-treated cells also decreases slightly, which can be attributed to the formation of GSH-conjugates

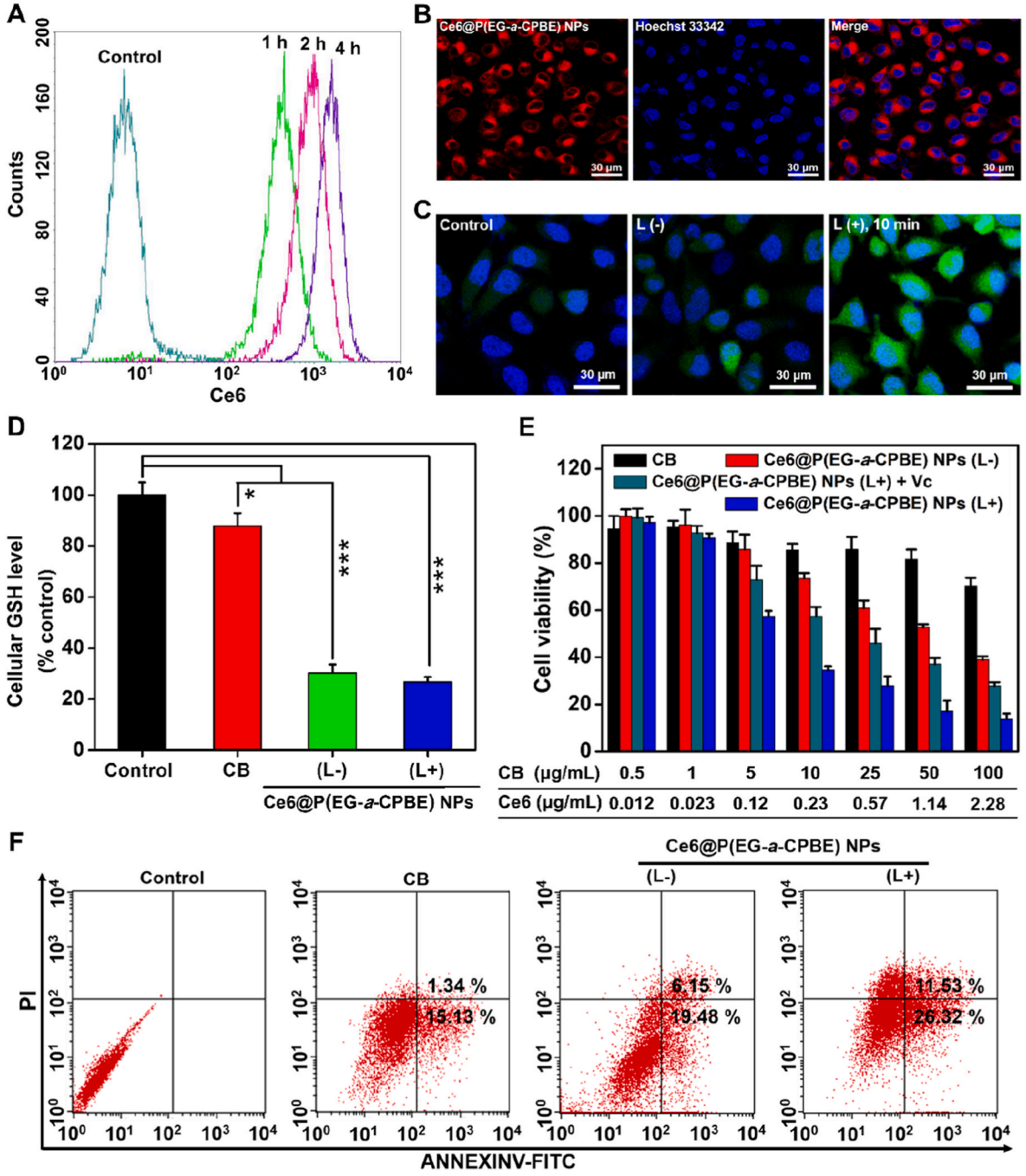

Fig. 3. *In vitro* evaluation of Ce6@P(EG-*a*-CPBE) NPs. (**A**) The flow cytometry diagram of MCF-7 cells treated with Ce6@P(EG-*a*-CPBE) NPs for 1 h, 2 h, and 4 h. The untreated cells are used as a control. (**B**) CLSM photos of MCF-7 cells cultured with Ce6@P(EG-*a*-CPBE) NPs for 4 h. The cell nuclei are stained with Hoechst 33,342. (**C**) CLSM images of MCF-7 cells treated by Ce6@P(EG-*a*-CPBE) NPs with (L+) or without (L-) 660 nm laser irradiation. (**D**) The level of GSH in MCF-7 cells after treatment with CB, Ce6@P(EG-*a*-CPBE) NPs (L-), and Ce6@P(EG-*a*-CPBE) NPs (L+) for 24 h. The level of GSH in the untreated group is set to 100%. $^{*}P < 0.05$, $^{***}P < 0.001$ (**E**) *In vitro* cytotoxicity of free CB, Ce6@P(EG-*a*-CPBE) NPs (L-) and Ce6@P(EG-*a*-CPBE) NPs (L+) to MCF-7 cells. The data are presented as average ± standard error (n = 5). (**F**) The cell apoptosis rate of MCF-7 cells induced by free CB, Ce6@P(EG-*a*-CPBE) NPs (L-) and Ce6@P(EG-*a*-CPBE) NPs (L+).

between GSH and CB [54]. Additionally, the cells treated with Ce6@P (EG-*a*-CPBE) NPs (L-) or Ce6@P(EG-*a*-CPBE) NPs (L+) show a similar decrease of GSH, suggesting the intracellular GSH has been depleted by P(EG-*a*-CPBE) prodrug completely, which inhibits them to scavenge the ROS generated by Ce6 under 660 nm laser irradiation, enhancing the efficacy of PDT. To confirm the synergetic effect, *in vitro* cytotoxicity of Ce6@P(EG-*a*-CPBE) NPs was evaluated against MCF-7 cells by methyl tetrazolium (MTT) assay, compared with that of free CB. After treatment with Ce6@P(EG-*a*-CPBE) NPs or free CB for 4 h, the medium was removed and the cells washed three times were irradiated by using 660 nm laser for 10 min and further cultured for 72 h at 37 °C for the MTT assay. As indicated in Fig. 3E, free CB inefficiently inhibited the growth of MCF-7 cells, while Ce6@P(EG-*a*-CPBE) NPs without laser irradiation show slightly enhanced inhibition activity of cancer cells, indicating that QM released from P(EG-*a*-CPBE) NPs could deplete GSH to induce tumor cells apoptosis, enhancing the efficacy of chemotherapy. Upon 660 nm laser irradiation, Ce6@P(EG-*a*-CPBE) NPs (L+) exhibited the highest anticancer activity, which can be ascribed to the ROS generated from Ce6 under 660 nm laser irradiation, meanwhile, intracellular GSH is effectively consumed by QM to prevent the depletion of ROS and

enhanced the synergistic chemo-photodynamic effect. However, the anticancer efficacy of Ce6@P(EG-*a*-CPBE) NPs (L+) is obviously decreased with the addition of ROS scavenger V_C, suggesting that the highest anticancer activity of Ce6@P(EG-*a*-CPBE) NPs (L+) is attributed to the combination of H_2O_2-triggered CB prodrug release and the $^1O_2$ generated from Ce6 under 660 nm laser irradiation.

In addition, cell apoptosis was also detected after treatment with different formulations by using the FITC-Annexin V/propidium iodide (PI) method. As shown in Fig. 3F, the free CB induces apoptosis in 16.47% of MCF-7 cells. The ratio of apoptotic cells is improved to 25.63% when the MCF-7 cells were incubated with Ce6@P(EG-*a*-CPBE) NPs (L-). Additionally, the highest apoptotic percentage of 37.85% can be achieved when the MCF-7 cells were treated with Ce6@P(EG-*a*-CPBE) NPs (L+), indicating that $^1O_2$ produced from Ce6 under 660 nm light irradiation can also induce cell apoptosis to achieve the synergistic chemo-photodynamic efficacy.

3.4. Pharmacokinetics and biodistribution studies

Compared to free small molecule drugs, polymer prodrug NPs usually have a longer retention time in the blood. To demonstrate this, the pharmacokinetics profile of Ce6@P(EG-*a*-CPBE) NPs was evaluated. The MCF-7 tumor-bearing mice were intravenously injected with Ce6@P(EG-*a*-CPBE) NPs or free CB, respectively. The plasma CB concentration versus time curves is indicated in Fig. 4A. Obviously, Ce6@P(EG-*a*-CPBE) NPs can significantly prolong the blood retention time of polymer prodrug containing CB compared to that of free CB, which would benefit the accumulation of them in tumor tissue.

To further test the amount of CB in tumor tissue and main organs, the MCF-7 tumor-bearing mice were intravenously injected with free CB or Ce6@P(EG-*a*-CPBE) NPs at an equivalent CB dosage of 10 mg kg^{-1}. After injection for different time intervals, the mice were sacrificed, and the tumor tissue and main organs were collected and homogenized. Subsequently, the drug was extracted with organic solvent for HPLC analysis. As shown in Fig. 4B, after injection with Ce6@P(EG-*a*-CPBE) NPs for either 2 h or 8 h, the accumulation of CB in tumor tissue is higher than that of free CB. Similar results can be observed in the main organs, including the liver, kidney, spleen, lung, and heart. Additionally, after injection with Ce6@P(EG-*a*-CPBE) NPs for 8 h, the accumulation of CB decreases remarkably in the spleen, lung, kidney, and liver, while the downward trend is slower in tumors.

To confirm the Ce6 encapsulated in P(EG-*a*-CPBE) NPs can efficiently accumulate in tumor tissue, *in vivo* fluorescence imaging of MCF-7 tumor-bearing mice was evaluated by detecting the fluorescence of Ce6 at different time points after intravenous injection via tail vein with free Ce6 or Ce6@P(EG-*a*-CPBE) NPs using a noninvasive optical imaging system (IVIS). As exhibited in Fig. 4C, the fluorescence signals of free Ce6 are distributed extensively in the whole body of the mouse within 1

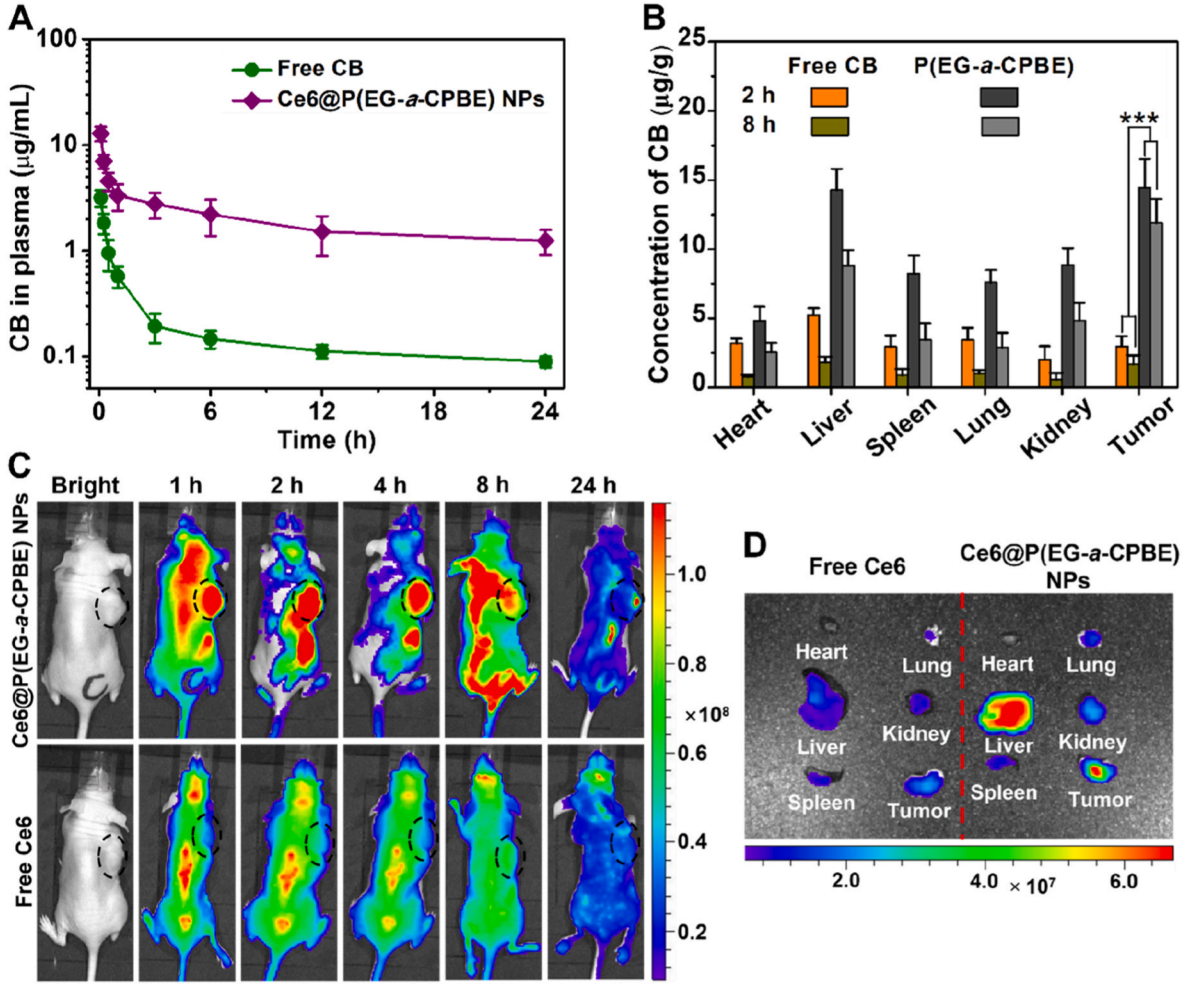

Fig. 4. *In vivo* pharmacokinetics and biodistribution evaluation of Ce6@P(EG-*a*-CPBE) NPs. (**A**) Plasma CB concentration after intravenous (*i.v.*) injection with free CB, or Ce6@P(EG-*a*-CPBE) NPs. The data are presented as the average ± standard error (n = 3). (**B**) Tissue distribution of CB, and P(EG-*a*-CPBE) NPs after intravenous injection with an equivalent concentration CB (10 mg kg^{-1}) of free CB and P(EG-*a*-CPBE) NPs in nude mice. Data are presented as average ± standard error (n = 3), and the statistical significance level is $^{***}P < 0.001$. (**C**) *In vivo* fluorescence images of MCF-7 tumor-bearing nude mice after intravenous (*i.v.*) injection with free Ce6 or Ce6@P(EG-*a*-CPBE) NPs. (**D**) Fluorescent photos of tumor and main organs after treatment with Ce6 or Ce6@P(EG-*a*-CPBE) NPs for 24 h.

h post-injection, while no obvious fluorescence signals were observed in the tumor site. After 24 h injection, the signals become extremely weak, indicating that free Ce6 is rapidly cleared from the bloodstream. On contrary, a strong fluorescence signal of Ce6 in Ce6@P(EG-*a*-CPBE) NPs is observed significantly in the tumor site after 1 h and then increases to the strongest at 2 h, suggesting the Ce6@P(EG-*a*-CPBE) NPs gradually accumulate in the tumor. Subsequently, the signal becomes gradually weak, while the signal in the tumor site still can be observed after 24 h post-injection. Additionally, the MCF-7 tumor-bearing mice were sacrificed, and the tumor tissue and main organs were stripped for the ex vivo fluorescence imaging after injection with free Ce6 or Ce6@P(EG-*a*-CPBE) NPs for 24 h using an *in vivo* imaging system. As displayed in Fig. 4D, compared to that treated with free Ce6, the tumor tissue exhibits a strong fluorescence signal of Ce6 after treatment with Ce6@P(EG-*a*-CPBE) NPs for 24 h, and the Ce6 fluorescence signals are also clearly observed in the liver.

3.5. *In vivo* anticancer activity

To further demonstrate the efficient accumulation of Ce6@P(EG-*a*-CPBE) NPs in tumors can enhance the synergetic anticancer activity, the MCF-7 tumor-bearing nude mice were intravenously injected with free CB or Ce6@P(EG-*a*-CPBE) NPs at an equivalent CB dose of 15.0 mg kg^{-1}. Under the guidance of fluorescence imaging, the whole tumor site was treated under 660 nm laser irradiation after injection for 2 h (Fig. 5A), and the mice untreated with laser irradiation were used as control. The tumor volume and body weight of mice were measured at every injection. As shown in Fig. 5B, the tumor volumes in mice treated with free CB and PBS are no significant difference, which may be ascribed to the insufficient accumulation of free CB in the tumor site. After treatment with Ce6@P(EG-*a*-CPBE) NPs (L-), the tumor volumes in mice are smaller than that of treatment with PBS, indicating that the CB can be efficiently delivered and accumulated in the tumor and the QM released from the linker PBA activated by H_2O_2 can deplete GHS causing the enhancement of chemotherapy efficacy. Upon irradiation with 660 nm laser at 2 h post-injection with Ce6@P(EG-*a*-CPBE) NPs, the tumor volumes in mice are the smallest than that of all treatments. Similar results were also contained by taking photos of tumors in mice in the process of therapy (Fig. 5E). After 24 days of injection, the mice were euthanized and the tumor tissues were isolated, washed with PBS, and photographed (Fig. 5F). The tumor tissues were weighed (Fig. 5C) to calculate the tumor inhibitory rate (TIR) (Fig. 5D). The TIR of the Ce6@P(EG-*a*-CPBE) NPs (L+) treatment group is 84.07 ± 5.85% compared with that of the PBS group, which is significantly higher than that of the Ce6@P(EG-*a*-CPBE) NPs (L-) treatment group (58.97 ± 3.21%) and free CB treatment group (20.05 ± 2.34%). These results demonstrate that the anticancer effect of Ce6@P(EG-*a*-CPBE) NPs (L+) is the highest in the all of treatment groups, which is mainly attributed to the combined therapeutic effect of quickly released CB and QM that depleted GSH to prevent the consumption of the generated ROS,

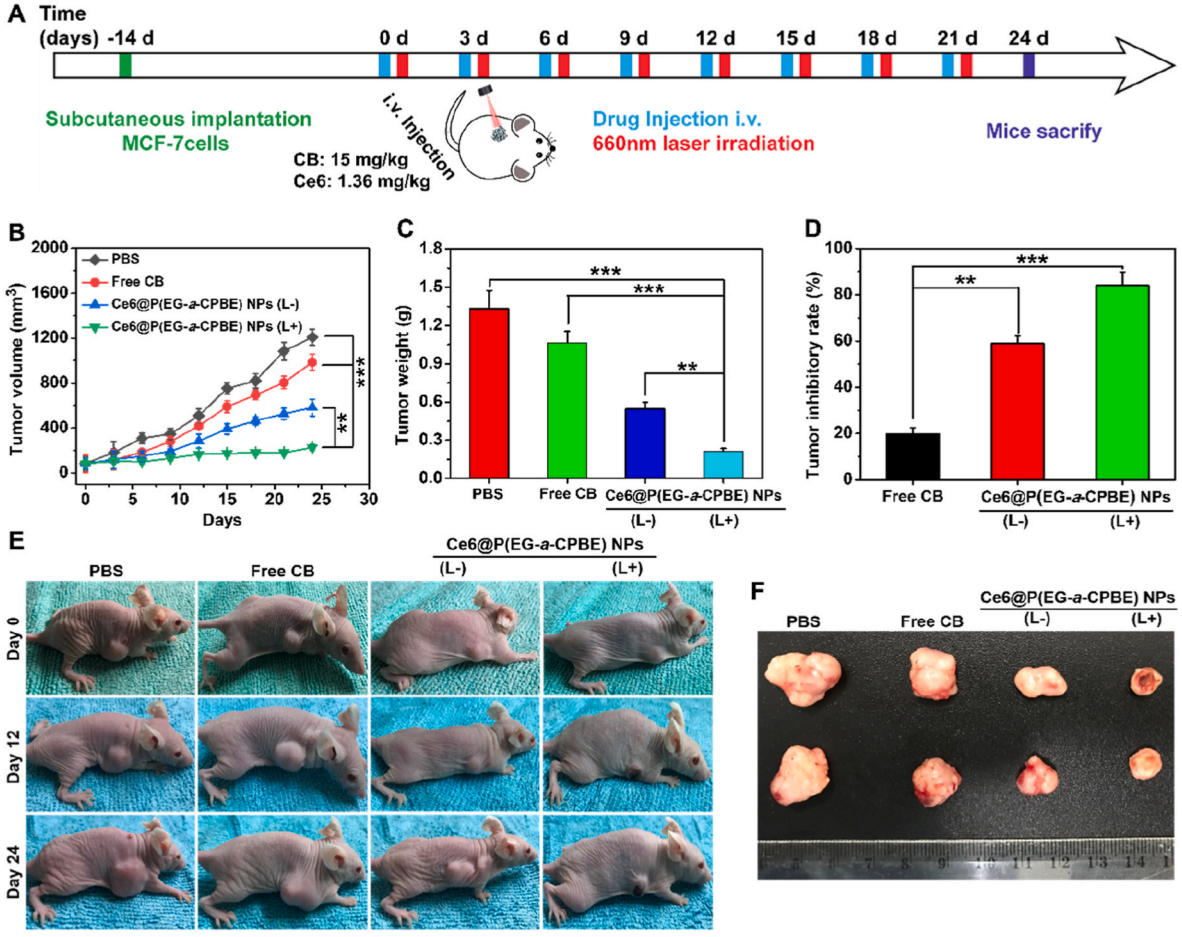

Fig. 5. *In vivo* antitumor activity. (**A**) Treatment schedule for MCF-7 tumor-bearing nude mice. (**B**) Changes in tumor volume of various groups in the therapeutic process. (**C**) The mean tumor weight in different treatment groups. (**D**) The tumor inhibitory rate (TIR) after treatment with different formulations. The TIR is calculated according to our previously reported method. Data are represented as average ± standard error (n = 5). Statistical significance: $^{**}P < 0.01$; $^{***}P < 0.001$. (**E**) The photo of MCF-7 tumor-bearing mice treated by different formulations during the 24-day therapeutic period. (**F**) Representative tumors isolated from mice at the end of therapy. For the laser irradiation group, the tumor sites were irradiated by 660 nm laser for 10 min after 2 h post-injection.

enhanced the antitumor efficacy of the combination of chemo-photodynamic therapy.

To further evaluate the anticancer effect of Ce6@P(EG-*a*-CPBE) NPs (L+), the tumor tissues were stripped and sectioned for the histopathological and immunohistochemical assay. The tissue sections stained by hematoxylin and eosin (H@E) indicate that large nucleus and spindle shape in the tumor tissues treated with PBS and free CB, while the number of tumor cells reduces obviously, and large nuclear shrinkage is observed in the group treated by Ce6@P(EG-*a*-CPBE) NPs, especially the group irradiation with 660 nm laser (Fig. 6A). Moreover, the cell proliferation in the tumor tissues was analyzed by use of proliferating cell nuclear antigen (PCNA) after treatment. As shown in Fig. 6B, the percentage of PCNA-positive (brown) tumor cells gradually reduces in the tumor tissues induced by free CB, Ce6@P(EG-a-CPBE) NPs (L-), and Ce6@P(EG-a-CPBE) NPs (L+) compared with that of the PBS group. Meanwhile, the quantitative analysis of the area percentage of PCNA-positive (brown) is obtained from Image J software and the results are shown in Fig. S11. It can be seen that the area percentage of PCNA-positive is 32.87%, 28.55%, and 18.44% treated by PBS, free CB, Ce6@P(EG-*a*-CPBE) NPs (L-) and significantly decreases to 3.36% if treatment with Ce6@P(EG-*a*-CPBE) NPs (L+). In contrast to other formulations, the Ce6@P(EG-*a*-CPBE) NPs (L+) can decrease much more PCNA-positive tumor cells, suggesting that the Ce6@P(EG-*a*-CPBE) NPs could achieve superiorly synergistic antitumor efficacy under irradiation with 660 nm laser.

In addition, the side effects of Ce6@P(EG-*a*-CPBE) NPs were investigated by checking the body weight change of mice and analyzing the pathological sections of main organs stained using H&E. As revealed in Fig. S12, no obvious body weight reduction of mice is observed in Ce6@P(EG-*a*-CPBE) NPs group with or without laser irradiation. Meanwhile, no obvious pathologic histological change is observed in the H&E-stained tissue sections of the heart, lung, spleen, liver, and kidney of the Ce6@P(EG-*a*-CPBE) NPs treatment with or without laser irradiation (Fig. S13), verifying the excellent biocompatibility of this polymer prodrug delivery system. Furthermore, serum biochemistry analysis was further performed to evaluate the biosafety of the Ce6@P(EG-*a*-CPBE) NPs. Generally, the liver is the major organ for nanoparticles elimination and thus causes inflammation easily. Figs. S14A and B displays no significant change in liver-function-related indexes, including alanine aminotransferase (ALT) and aspartate aminotransferase (AST) after treatment with the P(EG-*a*-CPBE) NPs and Ce6@P(EG-*a*-CPBE) NPs, indicating their low hepatotoxicity. The kidney is another main metabolic pathway for nanoparticles and undertakes a significant physiological burden. Therefore, kidney-function-related indexes, including blood urea nitrogen (BUN) and creatinine (CRE), were also analyzed and shows no obvious indication of kidney toxicity (Figs. S14C and D). All the above results confirm that such a prodrug delivery system has good biocompatibility and excellent biosafety.

4. Conclusion

In summary, we successfully designed and fabricated H_2O_2-responsive P(EG-*a*-CPBE) prodrug NPs to encapsulate Ce6 for chemo-photodynamic synergistic cancer therapy. The hydrophobic chemodrug CB was covalently linked to the side groups of hydrophilic alternating copolymer P(EG-*a*-PD) via an H_2O_2-cleavable PBA linker, and the obtained (EG-a-CPBE) prodrug could co-assemble with Ce6 to form Ce6@(EG-a-CPBE) prodrug NPs. The high stability of the PBA linker under a physiological environment could efficiently prevent premature drug leakage in blood circulation, reducing the side effect in normal tissue and cells. After accumulation of Ce6@(EG-a-CPBE) NPs in the tumor site and entering cells, the PBA rapidly cleaved triggered by endogenous H_2O_2 to release CB and Ce6, meanwhile, the PBA was also transformed into QM, which could consume intracellular GSH to prevent the ROS generated from Ce6 under 660 nm light irradiation to be depleted, achieving the combination of chemo-photodynamic therapeutic efficacy. Overall, such an H_2O_2-triggered prodrug and GSH-depleting agent release and activation strategy would offer a feasible approach to exploit the new generation nanodrugs with excellent biosafety and superior synergism of chemo-photodynamic therapy.

Ethics approval

All animal experiments were approved by the Animal Ethics Committee of Shanghai Jiao Tong University School of Medicine, and were performed in compliance with all relevant ethical regulations.

CRediT authorship contribution statement

Guanchun Wang: synthesized the polymer prodrug, prepared the Ce6@P(EG-a-CPBE) NPs, performed the chemical characterization, in vitro and in vivo anticancer activity evaluation, wrote the manuscript.

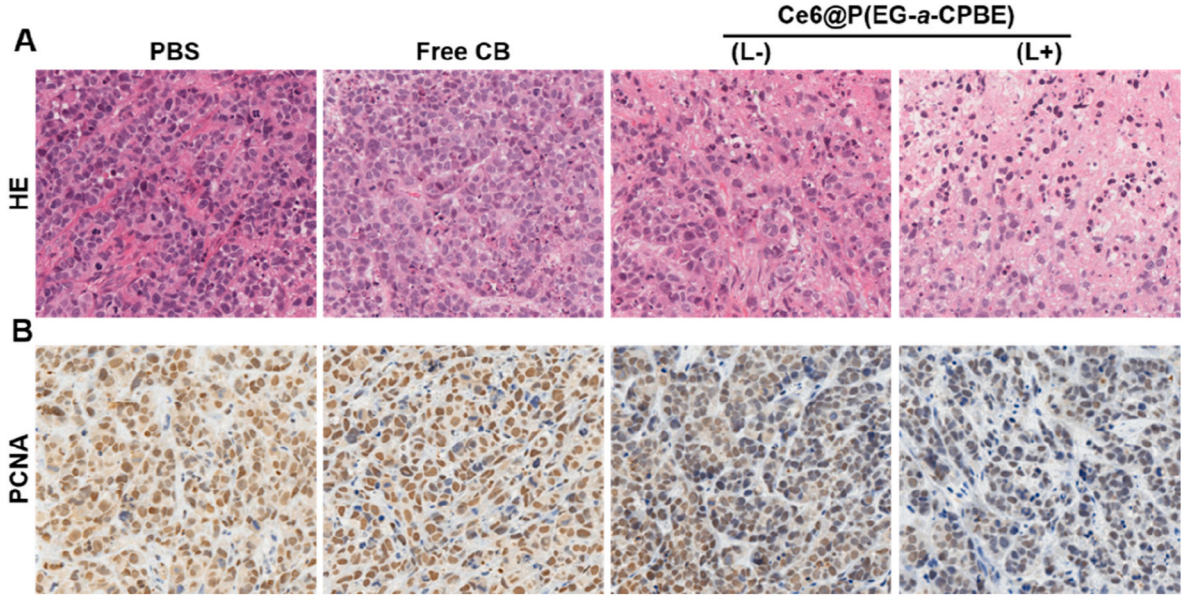

Fig. 6. H&E and PCNA analyses. (A) H&E and (B) PCNA analyses of MCF-7 tumor tissues after treatment with different formulations for 24 days.

Yue Su: helped with the cell experiment. **Xinliang Chen:** with the histological evaluation and analysis. **Yongfeng Zhou:** provided some guidances in this project. **Ping Huang:** designed the project and co-revised the manuscript. **Wei Huang:** designed the project and co-revised the manuscript. **Deyue Yan:** provided some guidances in this project.

Declaration of competing interest

The authors declare that they have no known competing financial interests or personal relationships that could have appeared to influence the work reported in this paper.

Acknowledgements

This work is supported by the National Natural Science Foundation of China (No. 22275122, No. 21702097, No. 21875134No. 52273281), the China Postdoctoral Science Foundation (No. 2020M671096), and the Medical Engineering Cross Project of Shanghai Jiao Tong University (No. YG2019ZDA05).

Appendix A. Supplementary data

Supplementary data to this article can be found online at https://doi.org/10.1016/j.bioactmat.2023.01.026.

References

[1] J.A. Hubbell, A. Chilkoti, Nanomaterials for drug delivery, Science 337 (2012) 303–305.
[2] V.P. Chauhan, R.K. Jain, Strategies for advancing cancer nanomedicine, Nat. Mater. 12 (2013) 958–962.
[3] M. Elsabahy, K.L. Wooley, Design of polymeric nanoparticles for biomedical delivery applications, Chem. Soc. Rev. 41 (2012) 2545–2561.
[4] K. Sakai-Kato, N. Nishiyama, M. Kozaki, T. Nakanishi, Y. Matsuda, M. Hirano, H. Hanada, S. Hisada, H. Onodera, H. Harashima, Y. Matsumura, K. Kataoka, Y. Goda, H. Okuda, T. Kawanishi, General considerations regarding the in vitro and in vivo properties of block copolymer micelle products and their evaluation, J. Contr. Release 210 (2015) 76–83.
[5] K.-J. Chen, L. Tang, M.A. Garcia, H. Wang, H. Lu, W.-Y. Lin, S. Hou, Q. Yin, C.K. F. Shen, J. Cheng, H.-R. Tseng, The therapeutic efficacy of camptothecin-encapsulated supramolecular nanoparticles, Biomaterials 33 (2012) 1162–1169.
[6] J. Xu, Q. Zhao, Y. Jin, L. Qiu, High loading of hydrophilic/hydrophobic doxorubicin into polyphosphazene polymersome for breast cancer therapy, Nanomedicine 10 (2014) 349–358.
[7] F. Zhou, B. Feng, T. Wang, D. Wang, Q. Meng, J. Zeng, Z. Zhang, S. Wang, H. Yu, Y. Li, Programmed multiresponsive vesicles for enhanced tumor penetration and combination therapy of triple-negative breast cancer, Adv. Funct. Mater. 27 (2017), 1606530.
[8] X. Xu, P.E. Saw, W. Tao, Y. Li, X. Ji, S. Bhasin, Y. Liu, D. Ayyash, J. Rasmussen, M. Huo, J. Shi, O.C. Farokhzad, ROS-responsive polyprodrug nanoparticles for triggered drug delivery and effective cancer therapy, Adv. Mater. 29 (2017), 1700141.
[9] H. Ringsdorf, Structure and properties of pharmacologically active polymers, J. Polym. Sci., Polym. Symp. 51 (1975) 135–153.
[10] C. Li, D.-F. Yu, R.A. Newman, F. Cabral, L.C. Stephens, N. Hunter, L. Milas, S. Wallace, Complete regression of well-established tumors using a novel water-soluble poly (L-glutamic acid)-paclitaxel conjugate, Cancer Res. 58 (1998) 2404–2409.
[11] J.W. Singer, Paclitaxel poliglumex (XYOTAX™, CT-2103): a macromolecular taxane, J. Contr. Release 109 (2005) 120–126.
[12] L.W. Seymour, D.R. Ferry, D. Anderson, S. Hesslewood, P.J. Julyan, R. Poyner, J. Doran, A.M. Young, S. Burtles, D.J. Kerr, Hepatic drug targeting: phase I evaluation of polymer-bound doxorubicin, J. Clin. Oncol. 20 (2002) 1668–1676.
[13] J.-Z. Du, X.-J. Du, C.-Q. Mao, J. Wang, Tailor-made dual pH-sensitive polymer–doxorubicin nanoparticles for efficient anticancer drug delivery, J. Am. Chem. Soc. 133 (2011) 17560–17563.
[14] H. Wang, X. Liu, Y. Wang, Y. Chen, Q. Jin, J. Ji, Doxorubicin conjugated phospholipid prodrugs as smart nanomedicine platforms for cancer therapy, J. Mater. Chem. B 3 (2015) 3297–3305.
[15] Q. Zhou, S. Shao, J. Wang, C. Xu, J. Xiang, Y. Piao, Z. Zhou, Q. Yu, J. Tang, X. Liu, Enzyme-activatable polymer–drug conjugate augments tumour penetration and treatment efficacy, Nat. Nanotechnol. 14 (2019) 799–809.
[16] P.D. Senter, E.L. Sievers, The discovery and development of brentuximab vedotin for use in relapsed Hodgkin lymphoma and systemic anaplastic large cell lymphoma, Nat. Biotechnol. 30 (2012) 631–637.
[17] C. Zhang, S. He, Z. Zeng, P. Cheng, K. Pu, Smart nano-PROTACs reprogram tumor microenvironment for activatable photo-metabolic cancer immunotherapy, Angew. Chem. Int. Ed. 61 (2022), e202114957.
[18] N. Ma, Y. Li, H. Xu, Z. Wang, X. Zhang, Dual redox responsive assemblies formed from diselenide block copolymers, J. Am. Chem. Soc. 132 (2010) 442–443.
[19] J. Wang, X. Sun, W. Mao, W. Sun, J. Tang, M. Sui, Y. Shen, Z. Gu, Tumor redox heterogeneity-responsive prodrug nanocapsules for cancer chemotherapy, Adv. Mater. 25 (2013) 3670–3676.
[20] D. Chen, G. Zhang, R. Li, M. Guan, X. Wang, T. Zou, Y. Zhang, C. Wang, C. Shu, H. Hong, Biodegradable, hydrogen peroxide, and glutathione dual responsive nanoparticles for potential programmable paclitaxel release, J. Am. Chem. Soc. 140 (2018) 7373–7376.
[21] Z. Deng, S. Liu, Controlled drug delivery with nanoassemblies of redox-responsive prodrug and polyprodrug amphiphiles, J. Contr. Release 326 (2020) 276–296.
[22] C. Luo, J. Sun, D. Liu, B. Sun, L. Miao, S. Musetti, J. Li, X. Han, Y. Du, L. Li, Self-assembled redox dual-responsive prodrug-nanosystem formed by single thioether-bridged paclitaxel-fatty acid conjugate for cancer chemotherapy, Nano Lett. 16 (2016) 5401–5408.
[23] C. Dong, Q. Zhou, J. Xiang, F. Liu, Z. Zhou, Y. Shen, Self-assembly of oxidation-responsive polyethylene glycol-paclitaxel prodrug for cancer chemotherapy, J. Contr. Release 321 (2020) 529–539.
[24] C. de Gracia Lux, S. Joshi-Barr, T. Nguyen, E. Mahmoud, E. Schopf, N. Fomina, A. Almutairi, Biocompatible polymeric nanoparticles degrade and release cargo in response to biologically relevant levels of hydrogen peroxide, J. Am. Chem. Soc. 134 (2012) 15758–15764.
[25] T.T. Hoang, T.P. Smith, R.T. Raines, A boronic acid conjugate of angiogenin that shows ROS-responsive neuroprotective activity, Angew. Chem., Int. Ed. 56 (2017) 2619–2622.
[26] X. Xia, X. Yang, P. Huang, D. Yan, ROS-responsive nanoparticles formed from RGD-epothilone B conjugate for targeted cancer therapy, ACS Appl. Mater. Interfaces 12 (2020) 18301–18308.
[27] W. Zhang, X. Hu, Q. Shen, D. Xing, Mitochondria-specific drug release and reactive oxygen species burst induced by polyprodrug nanoreactors can enhance chemotherapy, Nat. Commun. 10 (2019) 1–14.
[28] H. Jin, T. Zhu, X. Huang, M. Sun, H. Li, X. Zhu, M. Liu, Y. Xie, W. Huang, D. Yan, ROS-responsive nanoparticles based on amphiphilic hyperbranched polyphosphoester for drug delivery: light-triggered size-reducing and enhanced tumor penetration, Biomaterials 211 (2019) 68–80.
[29] J. Liu, Y. Pang, J. Chen, P. Huang, W. Huang, X. Zhu, D. Yan, Hyperbranched polydiselenide as a self assembling broad spectrum anticancer agent, Biomaterials 33 (2012) 7765–7774.
[30] C. Sun, Y. Tan, H. Xu, From selenite to diselenide-containing drug delivery systems, ACS Mater. Lett. 2 (2020) 1173–1177.
[31] Y. Li, Y. Li, W. Ji, Z. Lu, L. Liu, Y. Shi, G. Ma, X. Zhang, Positively charged polyprodrug amphiphiles with enhanced drug loading and reactive oxygen species-responsive release ability for traceable synergistic therapy, J. Am. Chem. Soc. 140 (2018) 4164–4171.
[32] J. Li, W. Ke, L. Wang, M. Huang, W. Yin, P. Zhang, Q. Chen, Z. Ge, Self-sufficing H2O2-responsive nanocarriers through tumor-specific H2O2 production for synergistic oxidation-chemotherapy, J. Contr. Release 225 (2016) 64–74.
[33] D. Lee, S. Khaja, J.C. Velasquez-Castano, M. Dasari, C. Sun, J. Petros, W.R. Taylor, N. Murthy, In vivo imaging of hydrogen peroxide with chemiluminescent nanoparticles, Nat. Mater. 6 (2007) 765–769.
[34] S. Park, J. Yoon, S. Bae, M. Park, C. Kang, Q. Ke, D. Lee, P.M. Kang, Therapeutic use of H2O2-responsive anti-oxidant polymer nanoparticles for doxorubicin-induced cardiomyopathy, Biomaterials 35 (2014) 5944–5953.
[35] M. Jiang, J. Mu, O. Jacobson, Z. Wang, L. He, F. Zhang, W. Yang, Q. Lin, Z. Zhou, Y. Ma, J. Lin, J. Qu, P. Huang, X. Chen, Reactive oxygen species activatable heterodimeric prodrug as tumor-selective nanotheranostics, ACS Nano 14 (2020) 16875–16886.
[36] Y. Wang, G. Wei, X. Zhang, F. Xu, X. Xiong, S. Zhou, A step-by-step multiple stimuli-responsive nanoplatform for enhancing combined chemo-photodynamic therapy, Adv. Mater. 29 (2017), 1605357.
[37] M. Yao, Y. Lu, L. Shi, Y. Huang, Q. Zhang, J. Tan, P. Hu, J. Zhang, G. Luo, N. Zhang, A ROS-responsive, self-immolative and self-reporting hydrogen sulfide donor with multiple biological activities for the treatment of myocardial infarction, Bioact. Mater. 9 (2022) 168–182.
[38] S.S. Lucky, K.C. Soo, Y. Zhang, Nanoparticles in photodynamic therapy, Chem. Rev. 115 (2015) 1990–2042.
[39] M. Wang, Y. Zhai, H. Ye, Q. Lv, B. Sun, C. Luo, Q. Jiang, H. Zhang, Y. Xu, Y. Jing, High co-loading capacity and stimuli-responsive release based on cascade reaction of self-destructive polymer for improved chemo-photodynamic therapy, ACS Nano 13 (2019) 7010–7023.
[40] P. Pei, C. Sun, W. Tao, J. Li, X. Yang, J. Wang, ROS-sensitive thioketal-linked polyphosphoester-doxorubicin conjugate for precise phototriggered locoregional chemotherapy, Biomaterials 188 (2019) 74–82.
[41] B. Chu, Y. Qu, X. He, Y. Hao, C. Yang, Y. Yang, D. Hu, F. Wang, Z. Qian, ROS-responsive camptothecin prodrug nanoparticles for on-demand drug Release and combination of chemotherapy and photodynamic therapy, Adv. Funct. Mater. 30 (2020), 2005918.
[42] C. Liang, L. Xu, G. Song, Z. Liu, Emerging nanomedicine approaches fighting tumor metastasis: animal models, metastasis-targeted drug delivery, phototherapy, and immunotherapy, Chem. Soc. Rev. 45 (2016) 6250–6269.
[43] J. Noh, B. Kwon, E. Han, M. Park, W. Yang, W. Cho, W. Yoo, G. Khang, D. Lee, Amplification of oxidative stress by a dual stimuli-responsive hybrid drug enhances cancer cell death, Nat. Commun. 6 (2015) 1–9.

[44] W. Yin, J. Li, W. Ke, Z. Zha, Z. Ge, Integrated nanoparticles to synergistically elevate tumor oxidative stress and suppress antioxidative capability for amplified oxidation therapy, ACS Appl. Mater. Interfaces 9 (2017) 29538–29546.
[45] J. Li, A. Dirisala, Z. Ge, Y. Wang, W. Yin, W. Ke, K. Toh, J. Xie, Y. Matsumoto, Y. Anraku, Therapeutic vesicular nanoreactors with tumor-specific activation and self-destruction for synergistic tumor ablation, Angew. Chem. 129 (2017) 14213–14218.
[46] H. Hagen, P. Marzenell, E. Jentzsch, F. Wenz, M.R. Veldwijk, A. Mokhir, Aminoferrocene-based prodrugs activated by reactive oxygen species, J. Med. Chem. 55 (2012) 924–934.
[47] G. Wang, P. Huang, M. Qi, C. Li, W. Fan, Y. Zhou, R. Zhang, W. Huang, D. Yan, Facile synthesis of a H2O2-responsive alternating copolymer bearing thioether side groups for drug delivery and controlled release, ACS Omega 4 (2019) 17600–17606.
[48] G. Wang, P. Huang, L. Wang, X. Chen, Y. Zhou, W. Huang, D. Yan, ROS-responsive thioether-containing hyperbranched polymer micelles for light-triggered drug release, Smartmat 3 (2022) 522–531.
[49] M. Wang, S. Sun, C.I. Neufeld, B. Perez-Ramirez, Q. Xu, Reactive oxygen species-responsive protein modification and its intracellular delivery for targeted cancer therapy, Angew. Chem., Int. Ed. 126 (2014) 13662–13666.
[50] S. Lee, A. Stubelius, N. Hamelmann, V. Tran, A. Almutairi, Inflammation-responsive drug-conjugated dextran nanoparticles enhance anti-inflammatory drug efficacy, ACS Appl. Mater. Interfaces 10 (2018) 40378–40387.
[51] C.-C. Song, R. Ji, F.-S. Du, D.-H. Liang, Z.-C. Li, Oxidation-accelerated hydrolysis of the ortho ester-containing acid-labile polymers, ACS Macro Lett. 2 (2013) 273–277.
[52] C.-Q. Luo, Y.-X. Zhou, T.-J. Zhou, L. Xing, P.-F. Cui, M. Sun, L. Jin, N. Lu, H.-L. Jiang, Reactive oxygen species-responsive nanoprodrug with quinone methides-mediated GSH depletion for improved chlorambucil breast cancers therapy, J. Contr. Release 274 (2018) 56–68.
[53] H. Wang, J.A. Joseph, Quantifying cellular oxidative stress by dichlorofluorescein assay using microplate reader, Free Radic. Biol. Med. 27 (1999) 612–616.
[54] D.S. Backos, C.C. Franklin, P. Reigan, The role of glutathione in brain tumor drug resistance, Biochem. Pharmacol. 83 (2012) 1005–1012.